Contents lists available at ScienceDirect

Optical Materials

Dispersion of the linear and nonlinear optical susceptibilities of Bismuth subcarbonate $Bi_2O_2CO_3$: DFT calculations

A.H. Reshak [a,b,*], S. Auluck [c]

[a] New Technologies – Research Centre, University of West Bohemia, Univerzitni 8, 306 14 Pilsen, Czech Republic
[b] Center of Excellence Geopolymer and Green Technology, School of Material Engineering, University Malaysia Perlis, 01007 Kangar, Perlis, Malaysia
[c] Council of Scientific and Industrial Research – National Physical Laboratory, Dr. K.S. Krishnan Marg, New Delhi 110012, India

ABSTRACT

The dispersion of the linear and nonlinear optical susceptibilities of bismuth subcarbonate $Bi_2O_2CO_3$ are calculated using density functional theory (DFT). We have employed the state-of-art all-electron full potential linearized augmented plane wave (FP-LAPW) method. Calculations are performed within the recently modified Becke–Johnson potential (mBJ) to obtain the self consistency conditions. The calculated linear optical susceptibilities exhibit a considerable anisotropy which is useful for second harmonic generation (SHG) and optical parametric oscillation (OPO). The calculated absorption coefficient show good agreement with the available experimental data. The values of calculated uniaxial anisotropy $\delta\varepsilon = -0.168$ and the birefringence $\Delta n(0) = 0.166$ indicate considerable anisotropy. The calculated SHG of the dominant component $\left|\chi_{322}^{(2)}(\omega)\right|$ is about $d_{32} = 5.3$ pm/V at $\lambda = 1064$ nm (1.165 eV) which is in excellent agreement with the available experimental data ($d_{32} = 5.49$ pm/V) obtained using pulsed Nd:YAG laser at wavelength $\lambda = 1064$ nm (10 ns, 3 mj 10 kHz). To analyze the origin of the high SHG of bismuth subcarbonate $Bi_2O_2CO_3$ we have correlated the features of $\left|\chi_{322}^{(2)}(\omega)\right|$ spectra with the features of $\varepsilon_2(\omega)$ spectra as a function of $\omega/2$ and ω.

© 2014 Elsevier B.V. All rights reserved.

1. Introduction

The nonlinear optical (NLO) materials have been extensively investigated because of their potential applications in nonlinear optics and laser engineering, for example borate materials BaB_2O_4, LiB_3O_5, CsB_3O_5, and $YCa_4(BO_3)_3O$ are all well-known NLO crystals [1] which show excellent properties such as short growth period, large effective nonlinear coefficient, high damage threshold, and good mechanical properties. Borate crystals exhibit huge NLO properties, particularly for second harmonic generation (SHG) and third harmonic generation (THG) applications [2–5]. It has been shown that anionic groups and chemical bonding structures of B atoms have a major influence on the NLO properties of borate crystals, that could be the reason of the high NLO properties [6,7]. Several other promising materials may also be found in more complex borates incorporating bismuth together with other cationic elements. For instance, several bismuth-containing borates crystallize in non-centro-symmetric space groups have been synthesized,

including $BaBiBO_4$, $Bi_2ZnB_2O_7$, $CaBiGaB_2O_7$, $Bi_2CaB_2O_7$, and $Bi_2SrB_2O_7$ [8–10]. These materials exhibit high NLO properties.

Further insight into the electronic structures and the physical properties of materials can be obtained from the calculations of interband optical functions. Bismuth subcarbonate $Bi_2O_2CO_3$ is particularly interesting for its high NLO properties, which could be related to the existing of $[CO_3]$ groups [11–13] and the p-cations with stereochemically active lone pairs $[Bi^{3+}]$ [14–16]. Also their considerable anisotropy leads to increase in the optical susceptibilities. Thus one requires reliable information about the optical functions. Therefore, based on our previous works [17–23] we have calculated the linear and nonlinear optical susceptibilities using the state-of-the-art full potential linear augmented plane wave (FPLAPW) method on several systems whose linear and nonlinear optical susceptibilities are known experimentally. We find very good agreement with the experimental data. Thus, we believe that our calculations reported in this paper would produce very accurate and reliable results.

To our knowledge no first-principles calculations on Bismuth subcarbonate $Bi_2O_2CO_3$ appeared so far in literature. Therefore a detailed depiction of the linear and nonlinear optical properties of bismuth subcarbonate $Bi_2O_2CO_3$ is timely and will bring us important insights to understand the electronic origins of huge linear and

* Corresponding author at: New Technologies – Research Centre, University of West Bohemia, Univerzitni 8, 306 14 Pilsen, Czech Republic.
E-mail address: maalidph@yahoo.co.uk (A.H. Reshak).

nonlinear optical susceptibilities by employing first-principles calculations using the full potential linear augmented plane wave (FP-LAPW) method which has proven to be one of the most accurate methods [24,25] for the computation of the electronic structure of solids within density functional theory (DFT). In this paper we address our selves to report these calculations based on the experimental results [26] so as to make a meaningful comparison.

2. Details of calculation

As starting point for our calculations, we have used the X-ray diffraction data taken from Huang et al. [26]. Bismuth subcarbonate $Bi_2O_2CO_3$ crystallizes in non-centro-symmetric orthorhombic space group Imm2, the lattice parameters are $a = 3.8658$ (5) Å, $b = 3.8648$ (5) Å, $c = 13.6757$ (5) Å and $z = 2$ [26]. The crystal structure of bismuth subcarbonate $Bi_2O_2CO_3$ along a-, b-, c-axis are presented in Fig. 1. The structure was optimized by minimization of the forces (1 mRy/au) acting on the atoms using Perdew–Burke–Ernzerhof generalized gradient approximation (GGA) [27]. Once the forces are minimized in this construction one can then find the self-consistent density at these positions by turning off the relaxations and driving the system to self-consistency. We have employed the state-of-the-art full potential linear augmented plane wave (FPLAPW) method in a scalar relativistic version as embodied in the WIEN2k code [28]. This is an implementation of the density functional theory (DFT) [29]. Exchange and correlation potential was described by the modified Becke–Johnson potential (mBJ) [30]. The Kohn–Sham equations are solved using a basis of linear APW's. The potential and charge density in the muffin-tin (MT) spheres are expanded in spherical harmonics with $l_{max} = 8$ and nonspherical components up to $l_{max} = 6$. In the interstitial region the potential and the charge density are represented by Fourier series. Self-consistency is obtained using 200 k points in the irreducible Brillouin zone (IBZ). We have calculated the linear optical susceptibilities using 500 k points in the IBZ, while for the nonlinear optical susceptibilities a mesh of 1500 k points was used.

The orthorhombic symmetry allows only three non-zero components of the second-order optical dielectric tensor components corresponding to the electric field $\vec{E}$ being directed along **a**, **b**, and **c**-crystallographic axes. We identify these with the x, y and z Cartesian directions. Therefore, the complex tensor components consist of $\varepsilon^{xx}(\omega)$, $\varepsilon^{yy}(\omega)$ and $\varepsilon^{zz}(\omega)$ for different incident light polarizations ([1 0 0], [0 1 0] and [0 0 1], with respect to the crystalline axes). The imaginary part of the optical dielectric function's dispersion $\varepsilon_2^{xx}(\omega)$, $\varepsilon_2^{yy}(\omega)$ and $\varepsilon_2^{zz}(\omega)$ completely defines the linear optical properties. The imaginary part was calculated using the following expression taken from Ref. [31]:

$$\varepsilon_2^{ij}(\omega) = \frac{8\pi^2\hbar^2 e^2}{m^2 V} \sum_k \sum_{cv} (f_c - f_v) \frac{p_{cv}^i(k) p_{vc}^j(k)}{E_{vc}^2} \delta[E_c(k) - E_v(k) - \hbar\omega]$$

(1)

where m, e and $\hbar$ are the electron mass, charge and Planck's constant, respectively. f_c and f_v represent the Fermi distributions of the conduction and valence bands, respectively. The term $p_{cv}^i(k)$ denotes the momentum matrix element transition from the energy level c of the conduction band to the level v of the valence band at certain **k**-point in the BZ and V is the unit cell volume.

The complex second-order nonlinear optical susceptibility tensor $\chi_{ijk}^{(2)}(-2\omega;\omega;\omega)$ generally written as [32–35]:

$$\chi_{inter}^{ijk}(-2\omega,\omega,\omega) = \frac{e^3}{\hbar^2}\sum_{nml}\int\frac{d\vec{k}}{4\pi^3}\frac{\vec{r}_{nm}^i\{\vec{r}_{ml}^j\vec{r}_{ln}^k\}}{(\omega_{ln}-\omega_{ml})}\left\{\frac{2f_{nm}}{(\omega_{mn}-2\omega)}+\frac{f_{ml}}{(\omega_{ml}-\omega)}+\frac{f_{ln}}{(\omega_{ln}-\omega)}\right\}$$

(2)

$$\chi_{intra}^{ijk}(-2\omega,\omega,\omega) = \frac{e^3}{\hbar^2}\int\frac{d\vec{k}}{4\pi^3}\left[\sum_{nml}\omega_{nm}\vec{r}_{nm}^i\{\vec{r}_{ml}^j\vec{r}_{ln}^k\}\right.$$
$$\times\left\{\frac{f_{nl}}{\omega_{ln}^2(\omega_{ln}-\omega)}-\frac{f_{lm}}{\omega_{ml}^2(\omega_{ml}-\omega)}\right\}-8i\sum_{nm}\frac{f_{nm}\vec{r}_{nm}^i\{\Delta_{nm}^j\vec{r}_{nm}^k\}}{\omega_{mn}^2(\omega_{mn}-2\omega)}$$
$$\left.+2\sum_{nml}\frac{f_{nm}\vec{r}_{nm}^i\{\vec{r}_{ml}^j\vec{r}_{ln}^k\}(\omega_{ml}-\omega_{ln})}{\omega_{mn}^2(\omega_{mn}-2\omega)}\right]$$

(3)

$$\chi_{mod}^{ijk}(-2\omega,\omega,\omega) = \frac{e^3}{2\hbar^2}\int\frac{d\vec{k}}{4\pi^3}\left[\sum_{nml}\frac{f_{nm}}{\omega_{mn}^2(\omega_{mn}-\omega)}\left\{\omega_{nl}\vec{r}_{lm}^i\{\vec{r}_{mn}^j\vec{r}_{nl}^k\}-\omega_{lm}\vec{r}_{nl}^i\{\vec{r}_{lm}^j\vec{r}_{mn}^k\}\right\}\right.$$
$$\left.-i\sum_{nm}\frac{f_{nm}\vec{r}_{nm}^i\{\vec{r}_{mn}^j\Delta_{mn}^k\}}{\omega_{mn}^2(\omega_{mn}-\omega)}\right]$$

(4)

From these formulae we can notice that there are three major contributions to $\chi_{ijk}^{(2)}(-2\omega;\omega;\omega)$: the inter-band transitions $\chi_{inter}^{ijk}(-2\omega;\omega,\omega)$, the intra-band transitions $\chi_{intra}^{ijk}(-2\omega;\omega,\omega)$ and the modulation of inter-band terms by intra-band terms $\chi_{mod}^{ijk}(-2\omega;\omega,\omega)$, where $n \neq m \neq l$. Here n denotes the valence states, m the conduction states and l denotes all states ($l \neq m, n$). There are two kinds of transitions that can take place, one of them vcc', involves one valence band (v) and two conduction bands (c and c'), and the second transition $vv'c$, involves two valence bands (v and v') and one conduction band (c). The symbols are defined as $\Delta_{nm}^i(\vec{k}) = \vartheta_{nn}^i(\vec{k}) - \vartheta_{mm}^i(\vec{k})$ with $\vec{\vartheta}_{nm}^i$ being the i component of the electron velocity given as $\vartheta_{nm}^i(\vec{k}) = i\omega_{nm}(\vec{k})r_{nm}^i(\vec{k})$ and $\{r_{nm}^i(\vec{k})r_{ml}^j(\vec{k})\} = \frac{1}{2}\left(r_{nm}^i(\vec{k})r_{ml}^j(\vec{k}) + r_{nm}^j(\vec{k})r_{ml}^i(\vec{k})\right)$. The position matrix elements between band states n and m, $r_{nm}^i(\vec{k})$, are calculated from the momentum matrix element P_{nm}^i using the relation [36]: $r_{nm}^i(\vec{k}) = \frac{P_{nm}^i(\vec{k})}{im\omega_{nm}(\vec{k})}$, with the energy difference between the states n and m given by $\hbar\omega_{nm} = \hbar(\omega_n - \omega_m)$. $f_{nm} = f_n - f_m$ is the difference of the Fermi distribution functions. i, j and k correspond to cartesian indices. It has been demonstrated by Aspnes [37] that only the one-electron virtual transitions (transitions between one valence band state and two conduction band states, vcc') give a
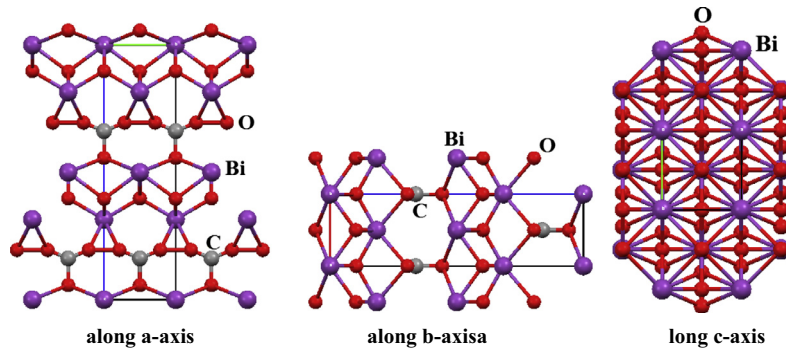
Fig. 1. Crystal structure of bismuth subcarbonate $Bi_2O_2CO_3$; (a) along a-axis; (b) along b-axis; (c) along c-axis.

significant contribution to the second-order tensor. We ignore the virtual-hole contribution (transitions between two valence band states and one conduction band state, $vv'c$) because it was found to be negative and more than an order of magnitude smaller than the virtual-electron contribution for this compound. For simplicity we denote $\chi_{ijk}^{(2)}(-2\omega; \omega; \omega)$ by $\chi_{ijk}^{(2)}(\omega)$. The subscripts i, j, and k are cartesian indices.

3. Results and discussion

3.1. Salient features of the electronic band structures

Since the optical properties is natural output of the calculated electronic band structure, therefore let us recall some salient features of the electronic band structure of bismuth subcarbonate $Bi_2O_2CO_3$. The calculated electronic structure along the optical transitions depicted on a generic band structure is represented in Fig. 2. It suggest that the conduction band minimum (CBM) and the valence band maximum (VBM) are situated at the centre of the BZ resulting in a direct band gap. The CBM is formed from Bi-s/p, O-p, C-p with negligible contribution from Bi-d/f, C-s and O-s states, whereas the VBM is formed by O-p, Bi-s/p, C-s/p with very small contribution of Bi-d/f and O-s states.

3.2. Linear optical response

The optical properties can provide detailed information about the electronic structure of the materials. The optical properties of solids are a major topic, both in basic research as well as for industrial applications. While for the former the origin and nature of different excitation processes is of fundamental interest, the latter can make use of them in many optoelectronic devices. Fig. 3a shows the calculated imaginary part of the dielectric function
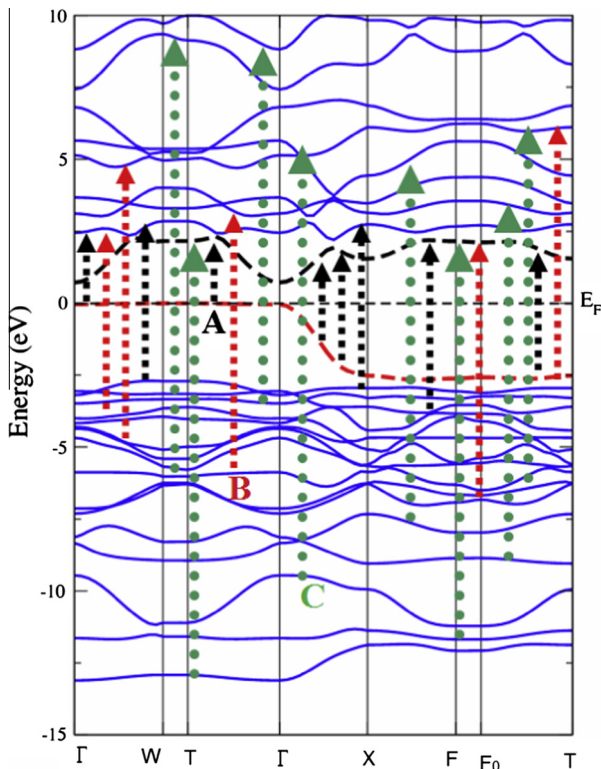
Fig. 2. The optical transitions depicted on a generic band structure of the bismuth subcarbonate $Bi_2O_2CO_3$.

versus the photon energy. The calculated optical spectra only include the direct inter-band transitions. Broadening is taken to be 0.1 eV which is traditional for oxide crystals and is typical of the experimental accuracy. All the optical properties are scissors corrected [38], more details about the scissors correction is give in Ref. [38]. Basically this increases the separation between the valence and conduction bands rigidly by the difference between the calculated (0.8 eV) and measured energy gaps (3.42 eV) [26]. It is a consequence of a fact that DFT calculations usually underestimate the energy gaps with respect to the experimental ones. A very simple way to overcome this drawback is to use the scissors correction factor, which merely brings the calculated energy gap close to the experimental one. The scissors correction can have a significant effect on the magnitude, peaks positions and the structure in general. This could arise from differences in the band structures and wave-functions. Following Fig. 3a one can see that the edge of optical absorption (fundamental absorption edge) for $\varepsilon_2^{xx}(\omega)$, $\varepsilon_2^{yy}(\omega)$ and $\varepsilon_2^{zz}(\omega)$ are situated at 3.42 eV. These edges of optical absorption give the threshold for direct optical transitions between the VBM and CBM. The electronic band structure suggests that the first spectral structure in $\varepsilon_2^{xx}(\omega)$, $\varepsilon_2^{yy}(\omega)$ and $\varepsilon_2^{zz}(\omega)$ is due to the transition from Bi-s/p/d, C-s/p and O-p to Bi-s/p, C-p/d and O-p states. The second structure corresponds to transition between Bi-s/p/d, C-s and O-p to Bi-s/d, C-s/p and O-p states. A remarkable fact regarding the first peak in $\varepsilon_2^{xx}(\omega)$, $\varepsilon_2^{yy}(\omega)$ and $\varepsilon_2^{zz}(\omega)$ is that its width is essentially determined by the width of the highest occupied valence band. We should emphasize that there exists a considerable anisotropy between the three principal complex tensor components, the anisotropy favors an enhanced phase matching conditions necessary for observation of the second harmonic generation (SHG) and optical parametric oscillation (OPO).

From the calculated imaginary part $\varepsilon_2^{xx}(\omega)$, $\varepsilon_2^{yy}(\omega)$ and $\varepsilon_2^{zz}(\omega)$ the real part $\varepsilon_1^{xx}(\omega)$, $\varepsilon_1^{yy}(\omega)$ can be obtained by means of Kramers–Kronig transformation [39] as shown in Fig. 3b. The vanishing frequency value in the dielectric function defines the static electronic dielectric constant by $\varepsilon_\infty = \varepsilon_1(0)$. These are $\varepsilon_1^{xx}(0) = 3.75$, $\varepsilon_1^{yy}(0) = 4.30$ and $\varepsilon_1^{zz}(0) = 3.55$. The uniaxial anisotropy $\delta\varepsilon = \left[(\varepsilon_0^{\parallel} - \varepsilon_0^{\perp})/\varepsilon_0^{tot} \right]$ is -0.168 indicating the existence of the considerable anisotropy. For more details about the optical properties and with the help of the existing information on the imaginary and real parts of the optical functions, we evaluate the reflectivity spectra $R(\omega)$, absorption coefficient $I(\omega)$, refractive indices $n(\omega)$ and the birefringence $\Delta n(\omega)$.

The reflectivity spectra for different incident light polarizations [1 0 0], [0 1 0] and [0 0 1], with respect to the crystalline axes is represented in Fig. 3c. At low energies the optical reflectivity starts at about 15% in the [1 0 0] direction, 16% along [0 1 0] direction and 18% along [0 0 1] direction. At the higher energies around 10.0 eV the investigated compound exhibits the higher reflectivity which forms the first reflectivity maximum by transition of s-states of VB to p-states of CB. At around 13.5 eV there existing an abrupt reduction in the reflectivity spectrum confirming the occurrence of a collective plasmon resonance. The depth of the plasmon minimum is determined by the imaginary part of the dielectric function at the plasma resonance and is representative of the degree of overlap between the inter-band absorption regions.

Fig. 3d represent the calculated absorption coefficient along [1 0 0], [0 1 0] and [0 0 1] directions, it shows the fundamental optical absorption edge located at 3.42 eV matching the experimental value of the absorption edge [26], see the small box inside Fig. 3d present the measured fundamental optical absorption edge which exhibit good agreement with our calculation. Then after there is a abrupt increases in the optical absorption to reach its maximum value at around 14.0 eV. It is necessary to mention that this compound possess wide optical transparency region (885–3625 Å).
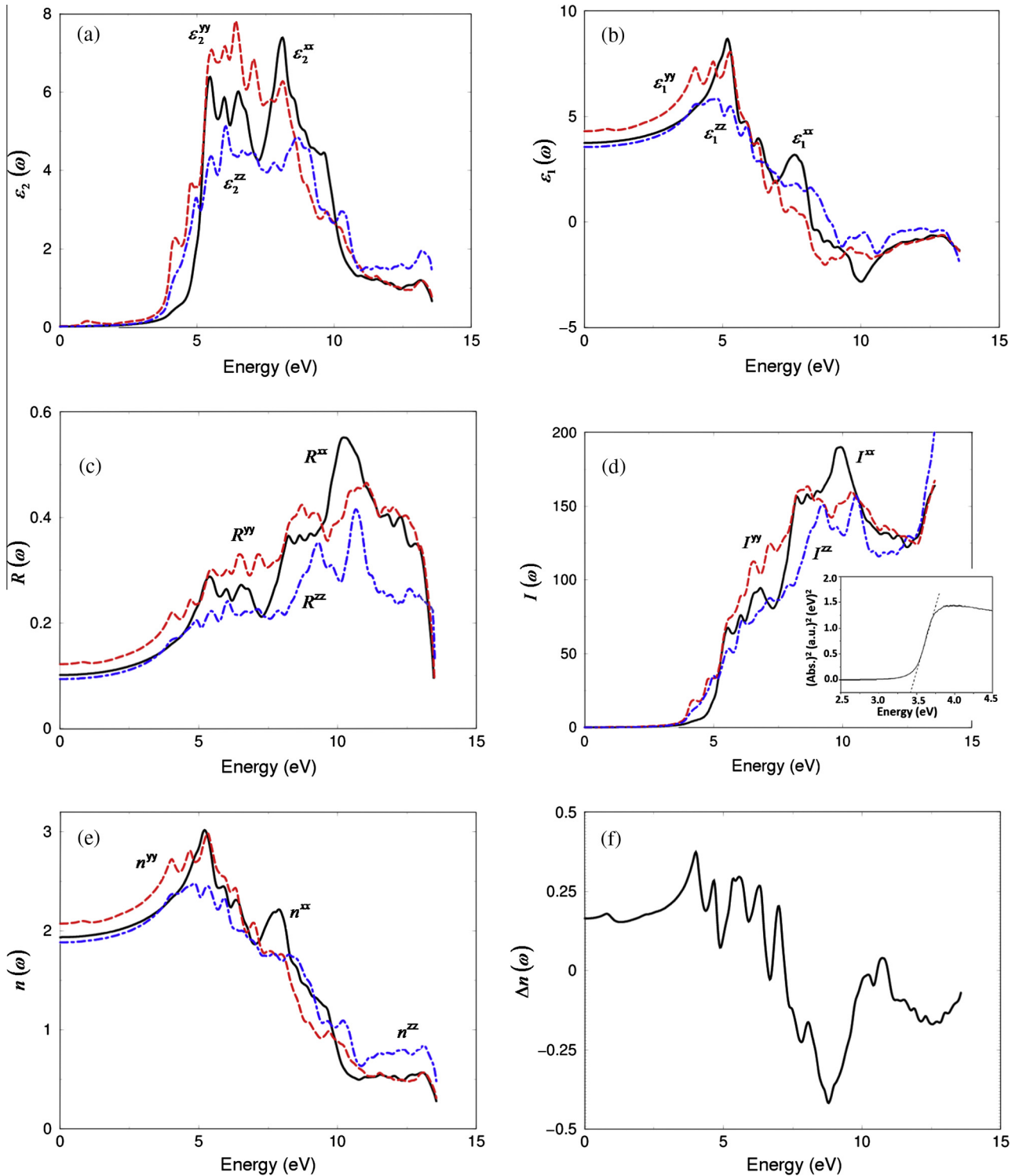
Fig. 3. (a) Calculated $\varepsilon_2^{xx}(\omega)$ (dark solid curve-black color online), $\varepsilon_2^{yy}(\omega)$ (light dashed curve-red color online) and $\varepsilon_2^{zz}(\omega)$ (light solid curve-blue color online) spectra. (b) Calculated $\varepsilon_1^{xx}(\omega)$ (dark solid curve-black color online), $\varepsilon_1^{yy}(\omega)$ (light dashed curve-red color online) and $\varepsilon_1^{zz}(\omega)$ (light solid curve-blue color online) spectra. (c) Calculated $R^{xx}(\omega)$ (dark dashed curve-black color online), $R^{yy}(\omega)$ (light solid curve-red color online), and $R^{zz}(\omega)$ (light solid curve-blue color online), along with our measured total $R(\omega)$ (dark solid curve-black color online). (d) Calculated absorption coefficient $I^{xx}(\omega)$ (dark solid curve-back color online), $I^{yy}(\omega)$ (light dashed curve-red color online) and $I^{zz}(\omega)$ (light solid curve-blue color online) spectrum. The absorption coefficient in 10^4 sec^{-1}. We should mention here that we compare our calculated results with the experimental data [26]. (e) Calculated refractive indices $n^{xx}(\omega)$ (dark solid curve-black color online), $n^{yy}(\omega)$ (light dashed curve-red color online) and $n^{zz}(\omega)$ (light solid curve-blue color online) spectrum. (f) Calculated birefringence $\Delta n(\omega)$. (For interpretation of the references to color in this figure legend, the reader is referred to the web version of this article.)

3.3. Refractive indices and birefringence

We have calculated the refractive indices $n^{xx}(\omega)$, $n^{yy}(\omega)$ and $n^{zz}(\omega)$ along [100], [010] and [001] directions as a function of

photon energy as illustrated in Fig. 3e. It can be seen that $n^{xx}(0)$, $n^{yy}(0)$ and $n^{zz}(0)$ at zero frequency show the static refractive index. They increase beyond the zero frequency limits and reached to their maximum values. Beyond the maximum value they start to

decrease and with few oscillations they go beyond unity. In this region ($n < 1$) the phase velocity of the photons increases to universal constant (C). However the group velocity always less than the C, therefore the relativity relations not effected [40]. To the best of our knowledge, there are no previous experimental or theoretical data for the refractive indices available in literature to make a meaningful comparison. Future experimental work will testify our calculated results. However we have done similar calculations on many compounds using DFT calculation within different exchange and correlation potentials. We find that the calculated refractive indices are in good agreement with experiment. In our recent publication on KTiOPO$_4$ (KTP) [41] BaBiBO$_4$ [42], Na$_3$La9O$_3$ (BO$_3$)$_8$ [17], BiB$_3$O$_6$ [43], CuInX$_2$ (X = S, Se, Te) [44], LiGaX$_2$ (X = S, Se) [45] we have compared the calculated refractive indices and the birefringence with experiment. For example we find that $n^{xx}(\omega)$ for KTP (at 1064 nm is calculated to be 1.746 and the experimental value varies from 1.738 to 1.782. Similar results are obtained for the other two directions. The calculated birefringence at 1064 nm is found to be 0.074. This is in good agreement with the experimental value of 0.084. Thus we can see that the obtained refractive indices are in good agreement with experiment. The refractive indices obtained using mBJ are expected to be much closer to the experimental values. The refractive indices show considerable anisotropy among $n^{xx}(\omega)$, $n^{yy}(\omega)$ and $n^{zz}(\omega)$ which is important for SHG and OPO as it is defined by the phase-matching condition. One can obtain the phase matching angle for the SHG (the angle between the optical beam and the optical axis for which the ω and 2ω beams are phase matched).

The birefringence can be evaluated from the linear response functions from which the anisotropy of the index of refraction is determined. The calculated birefringence is illustrated in Fig. 3f. The birefringence is defined as a difference between the extraordinary and ordinary refraction indices, $\Delta n(\omega) = n_e(\omega) - n_o(\omega)$, where $n_o(\omega)$ is the index of refraction for an electric field oriented along the c-axis (ordinary index of refraction) and $n_e(\omega)$ is the index of refraction for an electric field perpendicular to the c-axis (extraordinary index of refraction). It is clear that the birefringence is crucial only in the non-absorbing spectral range, which is below the energy gap. The value of the birefringence and the corresponding refractive indices at the static limit and at $\lambda = 1064$ nm (1.165 eV) are given in Table 1.

3.4. Second harmonic generation

The non-centro-symmetric orthorhombic space group Imm2, has several NLO parameters which are equal to zero. This symmetry allows only seven nonzero complex second-order nonlinear optical susceptibility tensors; $\chi^{(2)}_{113}(-2\omega;\omega;\omega) = \chi^{(2)}_{131}(-2\omega;\omega;\omega)$, $\chi^{(2)}_{223}(-2\omega;\omega;\omega) = \chi^{(2)}_{232}(-2\omega;\omega;\omega)$, $\chi^{(2)}_{311}(-2\omega;\omega;\omega)$, $\chi^{(2)}_{322}(-2\omega;\omega;\omega)$ and $\chi^{(2)}_{333}(-2\omega;\omega;\omega)$. For simplicity we can write the complex second-order nonlinear optical susceptibility tensor as $\chi^{(2)}_{ijk}(\omega)$. The

complex second-order nonlinear optical susceptibility tensors are more sensitive to the value of the band gap than the linear optical properties due to higher power energy differences in the denominators of the complex second-order nonlinear optical susceptibility tensors formalism given in Eqs. (2)–(4). To avoid the DFT drawback we consider a quasi-particle self-energy corrections at the level of scissors operators in which the energy bands are rigidly shifted to merely bring the calculated energy gap closer to the experimental gap. We should emphasize that the scissors corrections has a profound effect on the magnitude of $\left|\chi^{(2)}_{ijk}(\omega)\right|$. Fig. 4a represent the calculated $\left|\chi^{(2)}_{113}(\omega)\right|$, $\left|\chi^{(2)}_{223}(\omega)\right|$, $\left|\chi^{(2)}_{311}(\omega)\right|$, $\left|\chi^{(2)}_{322}(\omega)\right|$ and $\chi^{(2)}_{333}(\omega)$, which exhibit that the $\left|\chi^{(2)}_{322}(\omega)\right|$ tensor component give the highest value among the others, thus it is the dominant component at both the static limit and at 1.165 eV ($\lambda = 1064$ nm). These values are listed in Table 2, we noticed that the calculated SHG of the dominant component $\left|\chi^{(2)}_{322}(\omega)\right|$ is about $d_{32} = 5.3$ pm/V at $\lambda = 1064$ nm (1.165 eV) which is in excellent agreement with the available experimental data ($d_{32} = 5.49$ pm/V) using pulsed Nd:YAG laser at wavelength $\lambda = 1064$ nm (10 ns, 3 mj 10 kHz) [26]. The high SHG of Bismuth subcarbonate Bi$_2$O$_2$CO$_3$ could be related to the existing of [CO$_3$] groups which have planer structure with π-orbitals [11–13] and the p-cations with stereo-chemically active lone pairs [Bi^{3+}] which exhibit large distortion of Bi–O polyhedron [14–16]. Also due to their considerable anisotropy which led to increase the corresponding optical susceptibilities. We should emphasize that the anisotropy in the linear optical susceptibilities favors an enhanced phase matching conditions necessary for observation of the SHG. The static values of the second order susceptibility tensor are very important which can be use to estimate the relative SHG efficiency. We have calculated the dispersions of the imaginary and real parts of $\chi^{(2)}_{322}(\omega)$ as a function of photon energy (Fig. 4b). The imaginary and real parts consists of inter-band and intra-band contributions, in additional ω and 2ω resonances can be further separated into inter-band and intra-band contributions. Fig. 4c illustrated the total Im $\chi^{(2)}_{322}(\omega)$ a long with the $2\omega/\omega$ inter-/intra-band contributions. The imaginary part clearly show that $\chi^{(2)}_{ijk}(\omega)$ is zero below half the band gap, then after increases since the 2ω resonance begin to contribute at energies above half the band gap due to $E - 2\omega$ terms in the denominator of the above mentioned formalism (2)–(4). The ω resonance begins to contribute for energy values above the fundamental energy gap. We will use the absolute value of the dominant component $\left|\chi^{(2)}_{322}(\omega)\right|$ as prototype to analyze the features of the calculated $\chi^{(2)}_{113}(\omega)$, $\chi^{(2)}_{223}(\omega)$, $\chi^{(2)}_{311}(\omega)$, $\chi^{(2)}_{322}(\omega)$ and $\chi^{(2)}_{333}(\omega)$. To achieve that, the absorptive part of the corresponding dielectric function $\varepsilon_2(\omega)$ as a function of both $\omega/2$ and ω will be compare to $\left|\chi^{(2)}_{322}(\omega)\right|$ as shown in Fig. 4d. For simplicity we will divide the energy region into three parts. The first part from 1.71 up to 4.0 eV, contains the first structure of $\left|\chi^{(2)}_{322}(\omega)\right|$ which is originated from 2ω resonance. The second energetic part extended from 4.0 till 8.0 eV represents the second structure of $\left|\chi^{(2)}_{322}(\omega)\right|$ is associated with interference between 2ω and ω resonances (the threshold of $\varepsilon_2(\omega)$. Finally, the third part from 8.0 till 3.5 eV represent the spectral structure of $\left|\chi^{(2)}_{322}(\omega)\right|$ which is mainly due to ω resonance and is associated with the second structure in $\varepsilon_2(\omega)$.

4. Conclusions

As starting point for our calculation of the linear and nonlinear optical susceptibilities of bismuth subcarbonate Bi$_2$O$_2$CO$_3$ we have

Table 1
The calculated $\varepsilon_1^{xx}(0)$, $\varepsilon_1^{yy}(0)$, $\varepsilon_1^{zz}(0)$, $n^{xx}(0)$, $n^{yy}(0)$, $n^{zz}(0)$, and $\Delta n(0)$, at static limit and at $\lambda = 1064$ nm.

	At static limit	At $\lambda = 1064$ nm
$\varepsilon_1^{xx}(0)$	3.75	3.82
$\varepsilon_1^{yy}(0)$	4.30	4.35
$\varepsilon_1^{zz}(0)$	3.55	3.63
$n^{xx}(0)$	1.935	1.959
n^{yy}	2.074	2.088
n^{zz}	1.881	1.981
$\Delta n(0)$	0.166	0.118
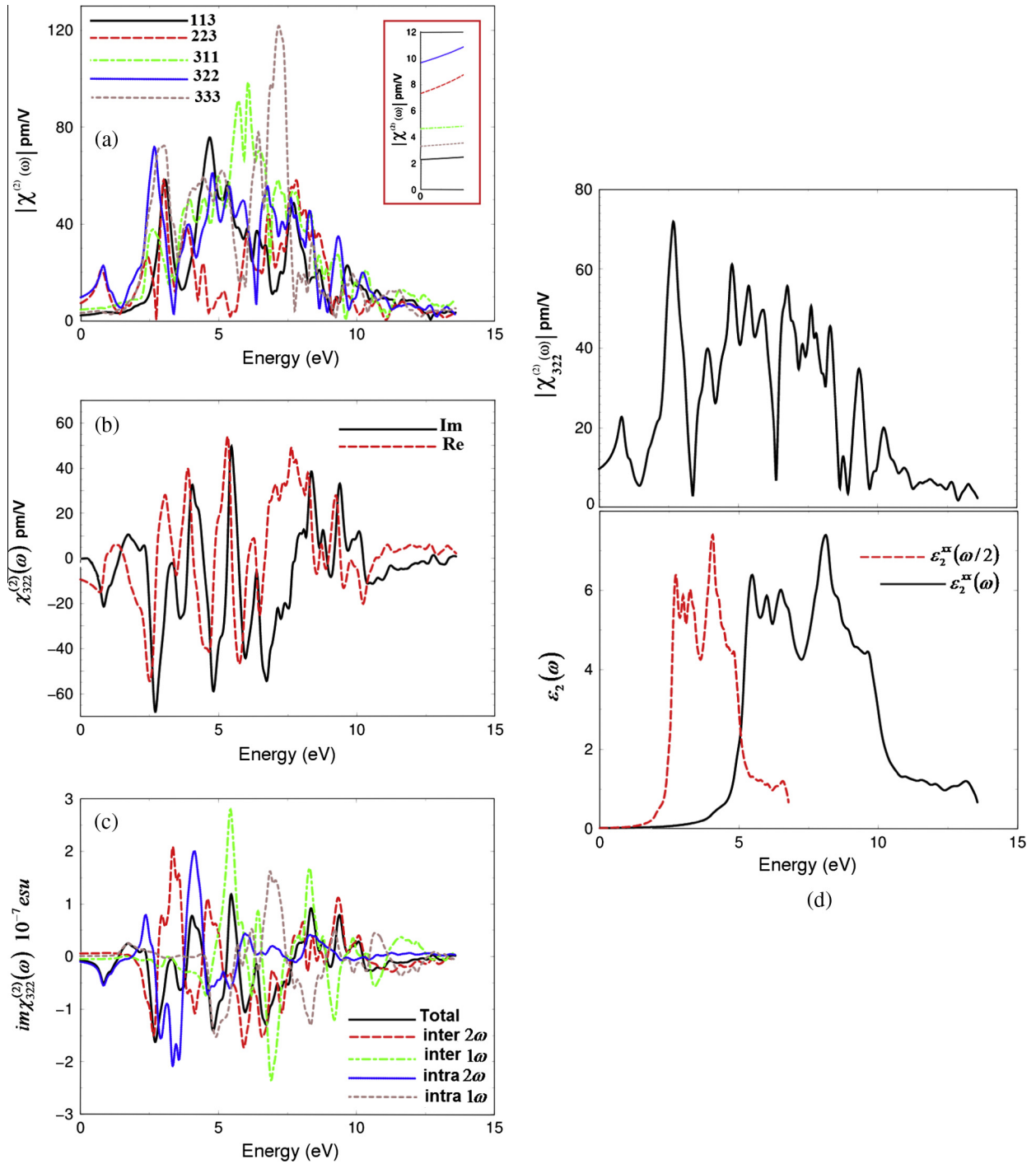
Fig. 4. (a) Calculated $\left|\chi_{ijk}^{(2)}(\omega)\right|$ for the five components using EVGGA with scissors correction. (b) Calculated Imaginary $\chi_{322}^{(2)}(\omega)$ (dark solid curve-black color online) and real $\chi_{333}^{(2)}(\omega)$ (light dashed curve-red color online) spectra, using mBJ with scissors correction; (c) calculated total Re $\chi_{322}^{(2)}(\omega)$ spectrum (dark solid curve-black color online) along with the intra $(2\omega)/(1\omega)$ (light solid curve-blue color online)/(light dashed doted curve-cyan color online) and inter $(2\omega)/(1\omega)$ (light long dashed curve-red color online)/ (light doted curve-green color online)-band contributions, here all Re $\chi_{333}^{(2)}(\omega)$ are multiplied by 10^{-7}, in esu units; (d) -*upper panel*- calculated $\left|\chi_{322}^{(2)}(\omega)\right|$ (dark solid curve-black color online) using mBJ with scissors correction; -*lower panel*- calculated $\varepsilon_2^{xx}(\omega)$ (dark solid curve-black color online); calculated $\varepsilon_2^{xx}(\omega/2)$ (dark dashed curve-red color online). (For interpretation of the references to color in this figure legend, the reader is referred to the web version of this article.)

used the X-ray diffraction data taken from recently synthesized bismuth subcarbonate $Bi_2O_2CO_3$ single crystal by Huang et al. Bismuth subcarbonate $Bi_2O_2CO_3$ crystallizes in non-centro-symmetric orthorhombic space group Imm2, this symmetry allows only three non-zero components of the second-order optical dielectric tensor components. Whereas for the nonlinear optical susceptibilities it allows seven nonzero complex second-order nonlinear optical susceptibility tensors. The calculations were performed using the state-of-the-art full potential linear augmented plane wave

(FPLAPW) method within the recently modified Becke–Johnson potential (mBJ). We present results for the imaginary, real parts of optical function's dispersion, reflectivity, absorption coefficient and the refractive indices spectra for different incident light polarizations [100], [010] and [001], with respect to the crystalline axes. From the calculated refractive indices we obtained the birefringence. The obtained values of the uniaxial anisotropy and the birefringence confirm the considerable anisotropy of bismuth subcarbonate $Bi_2O_2CO_3$ which is important for SHG as it is defined by

Table 2
Calculated $\left|\chi^{(2)}_{ijk}(\omega)\right|$ in pm/V at λ = 1064 nm along with measured values of d_{ijk} [26], where 1 pm/V = 2.387 × 10⁻⁹ esu.

Tensor components	Theory $\chi^{(2)}_{ijk}(\omega)$ in (pm/V) at static limit	Theory d_{ijk} = 0.5 $\chi^{(2)}_{ijk}(\omega)$ in (pm/V)	Theory $\chi^{(2)}_{ijk}(\omega)$ in (pm/V) at λ = 1064 nm	Theory d_{ijk} = 0.5 $\chi^{(2)}_{ijk}(\omega)$ in (pm/V) at λ = 1064 nm	Experiment at λ = 1064 nm in (pm/V)
$\left\|\chi^{(2)}_{113}(\omega)\right\|$	2.3	d_{15} = 1.15	3.4	d_{15} = 1.7	
$\left\|\chi^{(2)}_{223}(\omega)\right\|$	7.3	d_{24} = 3.65	6.6	d_{24} = 3.3	
$\left\|\chi^{(2)}_{311}(\omega)\right\|$	4.7	d_{31} = 2.35	6.0	d_{31} = 3.0	
$\left\|\chi^{(2)}_{322}(\omega)\right\|$	9.6	d_{32} = 4.8	10.6	d_{32} = 5.3	d_{32} = 5.49[a]
$\left\|\chi^{(2)}_{333}(\omega)\right\|$	3.3	d_{33} = 1.65	3.2	d_{33} = 1.60	

[a] Ref. [26].

the phase-matching condition. We have calculated the nonlinear optical susceptibilities namely the SHG, the obtained value of the dominant component (d_{32} = 5.3 pm/V) at λ = 1064 nm (1.165 eV) show excellent agreement with the measured value (d_{32} = 5.49 pm/V) using pulsed Nd:YAG laser at wavelength λ = 1064 nm (10 ns, 3 mj 10 kHz).

References

[1] P. Becker, Adv. Mater. Weinheim Ger. 10 (1998) 979.
[2] A. Brenier, I.V. Kityk, A. Majchrowski, Opt. Commun. 203 (2002) 125;
    A. Majchrowski, J. Kisielewski, E. Michalski, K. Ozga, I.V. Kityk, T. Lukasiewicz, Opt. Commun. 250 (2005) 334;
    I.V. Kityk, A. Majchrowski, Opt. Mater. 26 (2004) 33.
[3] B. Teng, J. Wang, Z. Wang, H. Jiang, X. Hu, R. Song, H. Liu, Y. Liu, J. Wei, Z. Shao, J. Cryst. Growth 224 (2001) 280.
[4] Z. Wang, B. Teng, K. Fu, X. Xu, R. Song, C. Du, H. Jiang, J. Wang, Y. Liu, Z. Shao, Opt. Commun. 202 (2002) 217;
    A.H. Reshak, S. Auluck, I.V. Kityk, A. Majchrowski, D. Kasprowicz, M. Drozdowski, J. Kisielewski, T. Lukasiewicz, E. Michalski, J. Mater. Sci. 41 (2006) 1927.
[5] Z. Lin, Z. Wang, C. Chen, M.H. Lee, J. Appl. Phys. 90 (2001) 5585.
[6] M. Ghotbi, Z. Sun, A. Majchrowski, E. Michalski, I.V. Kityk, Appl. Phys. Lett. 89 (2006) 173124.
[7] D. Xue, K. Betzler, H. Hesse, D. Lammers, Solid State Commun. 114 (2000) 21.
[8] J. Barbier, N. Penin, A. Denoyer, L.M.D. Cranswick, Solid State Sci. 7 (2005) 1055.
[9] J. Barbier, N. Penin, L.M. Cranswick, Chem. Mater. 17 (2005) 3130.
[10] J. Barbier, L.M.D. Cranswick, J. Solid State Chem. 179 (2006) 3958.
[11] G.H. Zou, N. Ye, L. Huang, X.S. Lin, J. Am. Chem. Soc. 133 (2011) 20001–20007.
[12] M. Luo, N. Ye, G.H. Zou, C.S. Lin, W.D. Cheng, Chem. Mater. 25 (2013) 3147–3153.

[13] T.T. Tran, P.S. Halasyamani, Inorg. Chem. 52 (2013) 2466–2473.
[14] Y.Z. Huang, L.M. Wu, X.T. Wu, L.H. Li, L. Chen, Y.F. Zhang, J. Am. Chem. Soc. 132 (2010) 12788–12789.
[15] S.D. Nguyen, J. Yeon, S.H. Kim, P.S. Halasyamani, J. Am. Chem. Soc. 133 (2011) 12422–12425.
[16] W.L. Zhang, W.D. Cheng, H. Zhang, L. Geng, C.S. Lin, Z.Z. He, J. Am. Chem. Soc. 132 (2010) 1508–1509.
[17] A.H. Reshak, S. Auluck, I.V. Kityk, J. Phys.: Condens. Matter 20 (2008) 145209.
[18] A.H. Reshak, S. Auluck, I.V. Kityk, J. Solid State Chem. 181 (2008) 789–795.
[19] A.H. Reshak, J. Chem. Phys. 124 (2006) 104707.
[20] A.H. Reshak, Eur. Phys. J. B 47 (2005) 503–508.
[21] A.H. Reshak, I.V. Kityk, S. Auluck, J. Phys. Chem. B 114 (2010) 16705–16712.
[22] A.H. Reshak, S. Auluck, D. Stys, I.V. Kityk, H. Kamarudin, J. Berdowski, Z. Tylczynskif, J. Mater. Chem. 21 (2011) 17219.
[23] A.H. Reshak, M. Piasecki, S. Auluck, I.V. Kityk, R. Khenata, B. Andriyevsky, C. Cobet, N. Esser, A. Majchrowski, M. S'wirkowicz, R. Diduszko, W. Szyrski, J. Phys. Chem. B 113 (46) (2009) 15237.
[24] Shiwu. Gao, Comput. Phys. Commun. 153 (2003) 190–198.
[25] Karlheinz. Schwarz, J. Solid State Chem. 176 (2003) 319–328.
[26] Hongwei. Huang, Na. Tian, Shifeng. Jin, Yihe. Zhang, Shuobo. Wang, Solid State Sci. 30 (2014) 1–5.
[27] J.P. Perdew, K. Burke, M. Ernzerhof, Generalized gradient approximation made simple, Phys. Rev. Lett. 77 (1996) 3865–3868.
[28] P. Blaha, K. Schwarz, G. K. H Madsen, D. Kvasnicka, J. Luitz, WIEN2k, An Augmented Plane Wave Plus Local Orbitals Program for Calculating Crystal Properties, Vienna University of Technology, Austria, 2001.
[29] P. Hohenberg, W. Kohn, Phys. Rev. B 136 (1964) 864.
[30] Fabien Tran, Peter Blaha, Phys. Rev. Lett. 102 (2009) 226401.
[31] F. Bassani, G.P. Parravicini, Electronic States and Optical Transitions in Solids, Pergamon Press Ltd., Oxford, 1975, pp. 149–154.
[32] S. Sharma, J.K. Dewhurst, C. Ambrosch-Draxl, Phys. Rev. B 67 (2003) 165332.
[33] A.H. Reshak, Ph.D. thesis, Indian Institute of Technology, Rookee, India, 2005.
[34] A.H. Reshak, J. Chem. Phys. 125 (2006) 014708.
[35] A.H. Reshak, J. Chem. Phys. 124 (2006) 014707.
[36] C. Ambrosch-Draxl, J. Sofo, Comp. Phys. Commun. 175 (2006) 1–14.
[37] D.E. Aspnes, Phys. Rev. B 6 (1972) 4648.
[38] Sergey N. Rashkeev, Walter R.L. Lambrecht, Phys. Rev. B 63 (2001) 165212;
    Sergey N. Rashkeev, Walter R.L. Lambrecht, B. Segall, Phys. Rev. B 57 (1998) 3905.
[39] H. Tributsch, Z. Naturforsch. A 32A (1977) 972.
[40] M. Fox, Optical Properties of Solids, Oxford University Press, 2001.
[41] A.H. Reshak, V. Kityk, S. Auluck, J. Phys. Chem. B 114 (2010) 16705–16712.
[42] Ali H. Reshak, S. Auluck, I.V. Kityk, J. Solid State Chem. 181 (2008) 789–795.
[43] A.H. Reshak, S. Auluck, I.V. Kityk, Appl. Phys. A 91 (2008) 451–457.
[44] A.H. Reshak, S. Auluck, PMC Phys. B 1 (2008) 12.
[45] A.H. Reshak, S. Auluck, I.V. Kityk, J. Alloys Compd. 473 (2009).